Automatic segmentation of coronary morphology using transmittance based lumen intensity-enhanced intravascular optical coherence tomography images and applying a localized level-set based active contour method

Shiju Joseph,[a] Asif Adnan,[a] and David Adlam[a]
[a]Department of Cardiovascular Sciences, University of Leicester, Leicester, U.K LE3 9QP

Abstract. Lumen segmentation from clinical intravascular optical coherence tomography (IV-OCT) images has clinical relevance as it provides a full three dimensional (3D) perspective of diseased coronary artery sections. Inaccurate segmentation may occur when there are artefacts in the image, resulting from issues such as inadequate blood clearance. This study proposes a transmittance based lumen intensity enhancement method that ensures lumen regions only are highlighted. A level-set based active contour method (ACM) that utilizes the local speckle distribution properties of the image, is then employed to drive an image-specific active contour towards the true lumen boundaries. By utilizing local speckle properties, the intensity variation issues within the image are resolved. This combined approach has been successfully applied to challenging clinical IV-OCT datasets that contains multiple lumens, residual blood flow and its shadowing artefact. A method to identify the guide-wire and interpolate the lost lumen segments has been implemented. This approach is fast and can perform even when guide-wire boundaries are not easily identified. Lumen enhancement also makes it easy to identify vessel side branches. This automated approach is not only able to extract the arterial lumen, but also the smaller microvascular lumens that are associated with the vasa vasorum and with atherosclerotic plaque.

Keywords: transmittance mapping, lumen segmentation, active contour, optical coherence tomography, Clinical applications..

Address all correspondence to: David Adlam, Department of Cardiovascular Sciences, University of Leicester, Leicester, U.K LE3 9QP; Tel: +44 116-204-4751; E-mail: da134@le.ac.uk

1 Introduction

Intravascular Optical Coherence Tomography (IV-OCT) is now widely used for the clinical assessment of atherosclerotic plaque, as this technology provides high-resolution (axially $\approx 15 \ \mu$m resolution) cross-sectional images of the coronary arterial wall.[1] While structural

1

images can provide a high-contrast view from these cross-sections, clinical image interpretation from 2-Dimensional sections requires considerable experience leading to significant inter-observer variability.[1] Automated assessment can reduce this error and produce more consistent image interpretation. Various techniques have been reported for lumen segmentation,[1–8] stent strut detection[7] and plaque characterization.[1,9] These approaches are either semi or fully automated.

Lumen segmentation and three dimensional (3D) reconstruction of the coronary artery has been a key objective due to the clinical applicability of this approach for the assessment and treatment of coronary stenosis. In IV- OCT images, lumen regions are visualized as a signal-sparse region surrounded by the bright tissue regions constituting the vessel wall. Thus, the wall-lumen interface provides a high degree of contrast and this is generally exploited by various techniques to extract the lumen boundary. Some of the methods previously employed, include: image thresholding,[1] A-line intensity-variation analysis,[2,3] intensity difference dependent cost function and its minimization approach[4,5] and labelling methods using Markov random field (MRF).[7] Alternatively, a combination approach with Expectation Maximization (EM) for labelling and graph-cut for lumen segmentation has been reported.[8] All these techniques use the tissue region as the reference from which to determine the boundary. The lumen geometry generated can then be refined using an active contour method (ACM).[6,8]
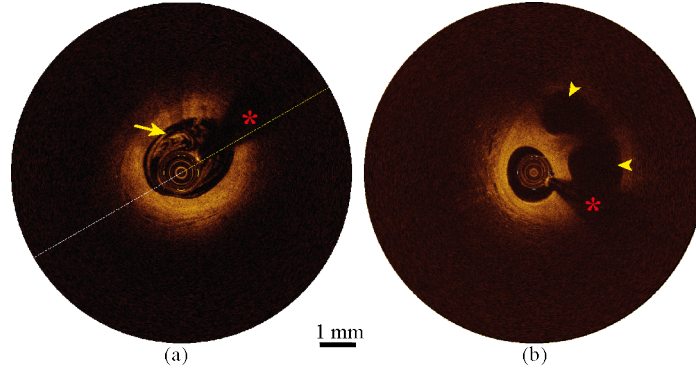
Fig 1 Examples of lumen segmentation challenges from in-vivo clinical IV-OCT images. (a) Residual blood circulation (arrow) within the lumen during imaging with associated shadowing artefact on the tissue region. (b) Image cross-section showing multiple lumens (arrow heads) in a diseased coronary section. The marking * indicates the guide-wire and its shadow artefact on the image.

The IV-OCT images in reports describing application of these lumen segmentation methods are usually selected to have optimal image quality. However, the real-world context of clinical IV-OCT frequently generates more challenging images resulting from complex anatomy, artefact and disease. For example, although rapid pullback technologies have eliminated the need for proximal balloon occlusion, during clinical image acquisition images are frequently partially distorted by blood artefact,[10] Fig.1. Additionally, diseased arteries may present highly altered lumen shapes (Fig.1) which can be challenging to current segmentation tools. Morphological operations,[6] prior to the lumen segmentation, can be applied to the IV-OCT images to minimise the effect of blood artefacts. However, complete removal is not guaranteed, especially when blood is flowing very close to, or in continuity with the luminal wall. In such situations cost function minimization methods[4,5] also fail and manual intervention is advised.[1,5] More importantly, when the intensity of tis-

3

sue region is reduced by the shadowing effect, intensity dependent segmentation methods may fail to distinguish the luminal region. In such situations, statistical property based labelling methods such as MRF[7] and EM+graph-cut,[8] may be able to identify tissue regions but systematic assessment of this strategy on challenging 'real world' clinical datasets is not reported. There is therefore a need for an automatic lumen segmentation tool that can account for such variations.

To create a fully automated lumen segmentation method, in this study a technique to enhance lumen intensity was applied , thereby focusing the segmentation approach on the lumen, instead of the tissue region. A statistically formulated level-set based ACM segmentation method was then employed to extract the lumen. To demonstrate the capability of this combined approach, challenging *in-vivo* clinical IV-OCT images with blood- flow artefacts and multiple lumens were successfully analysed. The proposed method is also capable of compensating for guide-wire artefact and yields the correct lumen contours for side-branch ostia.

2 Methods

Fig.2, illustrates the steps developed to automate the lumen segmentation process. Steps $1 - 5$ were implemented individually for each frame in the pullback dataset. The lumen region in every frame was enhanced and then a localized region based level-set segmentation method applied to segment the lumen. Once the lumen geometry was segmented
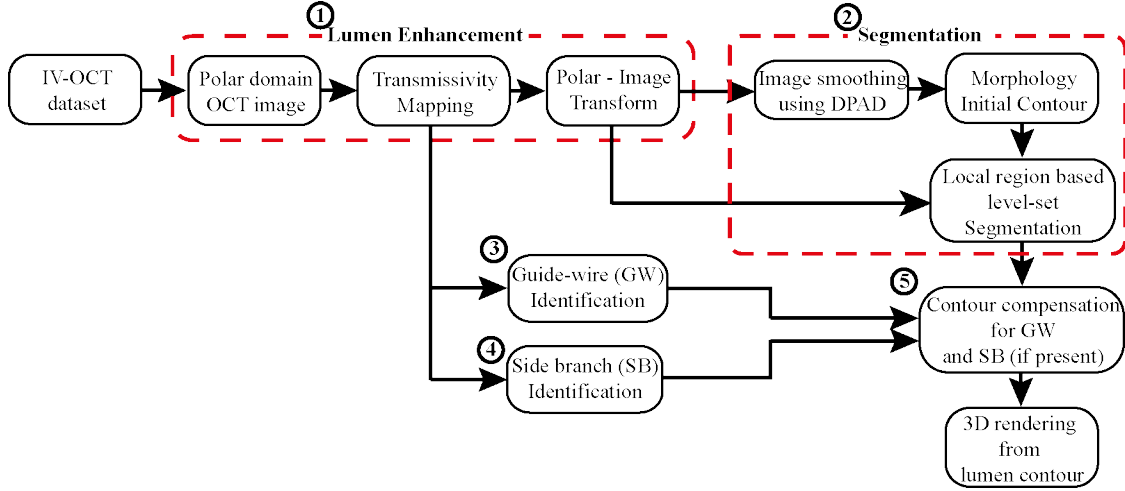
4

Fig 2 Block diagram illustrating the steps followed for segmenting the lumen from clinical *in-vivo* IV-OCT images. The encircled numerals 1 - 5 indicate the order of the steps. DPAD - detail preserving anisotropic diffusion.

from every frame, a 3-D vessel shape was rendered. The lumen enhancement method enabled the identification of guide-wire artefact and side-branch openings, which were then compensated after the lumen contour was obtained (see, Fig.2).

2.1 Transmissivity dependent intrinsic lumen contrast

An attenuation coefficient-based strategy has been widely used for OCT image enhancement[11] and also as a quantitative diagnostic parameter.[12] It has been employed for coronary artery tissue characterization[13] and classification of plaque constituents.[9,14] Due to blood clearance, luminal regions are largely devoid of any scattering material and therefore have very low attenuation coefficients, making this an ineffective contrasting agent. However, the reciprocal of attenuation coefficient gives the transmissivity of the region. Thus the

lower the attenuation, the higher the transmissivity and vice-versa. Subsequently, in a transmissivity map for an IV-OCT image, the luminal regions are expected to have bright contrast while tissue regions remain dark. This enables direct visualization of all lumen regions which can then be segmented with an appropriate technique.

The transmissivity (τ) map (inverse of attenuation coefficient), for a radial A-line was estimated using a depth resolved method,[11,12] given by

$$\tau(z) = \frac{1}{\mu(z)} = \frac{2 \int_z^\infty I(u)\, du}{I(z)}.$$ (1)

where, $\mu(z)$ is the attenuation coefficient, $I(z)$ is the OCT signal along the radial A-line of the IV-OCT image and z is the depth position. In Eq.1, it was assumed that all the light was attenuated within the imaging depth and also a certain fraction of attenuated light was always received at the detector. For practical implementation the infinity was replaced by total image depth, D. Since the transmissivity property was employed only to enhance the contrast of the luminal regions, so intensity exponentiation[11] was performed before a transmissivity calculation was implemented. Thus, Eq.1 becomes

$$\tau(z) = \frac{2 \int_z^D I^n(u)\, du}{I^n(z)}.$$ (2)

From Eq.2 it could be observed that the transmissivity map of a given IV-OCT image could change as the exponential factor, n was varied. Therefore, the effect of exponentiation on τ was analysed and also an appropriate value was determined that provided suitable
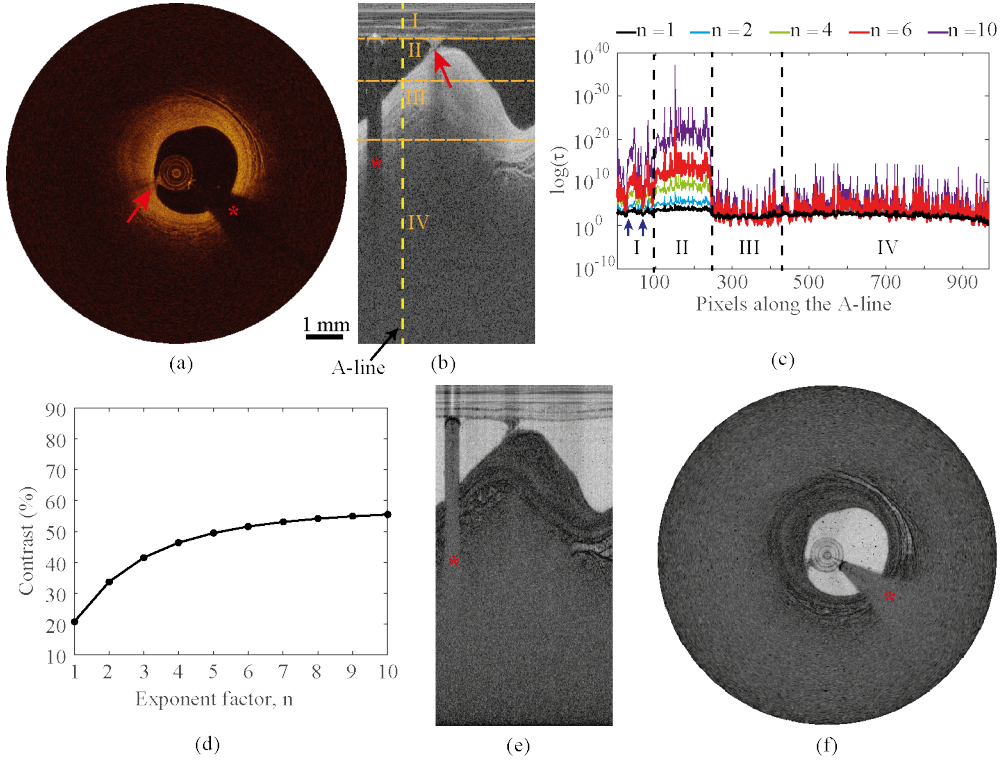
Fig 3 Transmittance dependent contrast generation and optimization for luminal region in an IV-OCT image.(a) *In-vivo* clinical IV-OCT image (b) Polar format image of (a). (c) Transmittance profile along the A-line marked in (b), for *n* different exponent values (in Eq. (2)). The sub-regions in (c) corresponds to areas marked in (b) where identifiers denote, I - catheter, II - lumen, III - tissue and IV - background. From (c) it is evident that, with increasing exponent value, the log-scale transmittance is mainly enhanced in the lumen. (d) Inter-layer contrast for *n* values, calculated using log-scale transmittance at lumen and background regions (respectively marked II and IV) along the A-line in (b). Contrast between the two layers increased with *n* value and at $n = 6, 50\%$ improvement in contrast was achieved. (e) Transmittance dependent intensity image of (b) obtained using $n = 6$. (f) Display format image of (e). Arrows in (a) and (b) points the blood volume between the wall and the catheter. The marking **＊** indicates the guide-wire.

contrast for the lumen.

The application and optimization of the technique is illustrated in Fig.3. Based on Eq. (2) a set of transmittance maps for Fig.3 were generated using $n = 1, 2, 4, 6, 10$ values. As shown in Fig.3(c) the log-scale compressed transmittance value for the lumen

regions (marked (II)) increased with the n value. Whereas, other regions such as tissue regions (marked (III) and background regions (marked (IV) had negligible changes when compared to lumen region. Though catheter region (marked (I) in Fig.3(c)) had transmissivity levels similar to the lumen region for a given n value, it did not affect the lumen segmentation.

From Fig.3(c), it was evident that increasing the exponential value improved both the τ value and the relative contrast of the lumen region. As the objective was to enhance the lumen contrast so the log-scale transmissivity values at lumen region were compared with the background region, as it had higher transmissivity when compare to tissue region. Using the below Eq. (3), inter-layer contrast was determined for every transmissivity map obtained for $n = 1, 2, ..., 10$.

$$C = \frac{\log(\tau_{lm}) - \log(\tau_{bg})}{\log(\tau_{lm}) - \log(\tau_{bg})} \times 100 \tag{3}$$

where, C was the calculated contrast in percentage, τ_{lm} and τ_{bg} respectively were the transmissivity value for selected region of interest (ROI) pixels in lumen and background regions. The mean of the $\log(\tau)$ value at (5×1) pixels for each region in the polar-format IV-OCT image were used. The plot in Fig.3(d) illustrates the change in the calculated contrast for various n values. The profile showed that the contrast improves non-linearly for $n \leq 6$ values, beyond which there was only minor improvement. Also, at $n = 6$ about 50% contrast was achieved which was found to be adequate enough to generate good lu-

8

men contrast as shown in Fig.3(e) and (f). The contrast profile shown in Fig.3(d) was generally observed for larger ROIs, albeit with only a change in the contrast values. Thus, throughout the study $n = 6$ was used to calculate the transmissivity coefficients for the IV-OCT images.

The transmissivity mapping method enabled selective enhancement of lumen intensity and the luminal regions were readily visualized. The catheter area, which had similar transmissivity as the lumen region, appeared as embedded within the later (as in Fig.3(f)). Therefore a direct segmentation of the lumen was now possible from display format images, without the need for sequential removal of catheter and its protective sheath.[4]

To obtain lumen intensity-enhanced IV-OCT images, first transmissivity maps were generated with $n = 6$ value, from every polar domain IV-OCT image. Then a log-scale compression was applied to the transmissivity maps, to reduce the dynamic range which was both inherently present and resulted from the exponentiation. The resultant was then converted to a 8-bit gray-scale intensity image. Thus obtained lumen intensity-enhanced polar-format images were transformed to image co-ordinates (Fig.3(f)).

2.1.1 Speckle analysis of lumen intensity-enhanced IV-OCT images

The lumen segmentation method employed in this study utilized the speckle distribution properties of the image. Therefore, a speckle analysis was carried out to determine the type of speckle distribution exhibited by the lumen intensity-enhanced IV-OCT image. Fig.4(a)
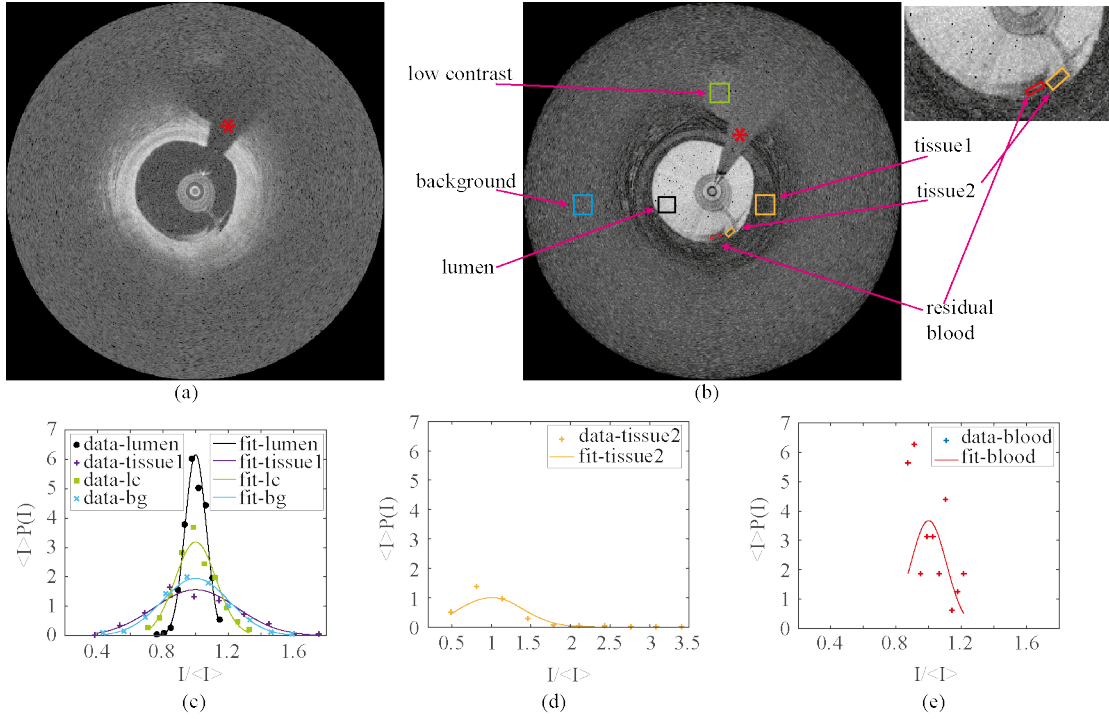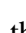
Fig 4 Speckle analysis of the lumen intensity-enhanced IV-OCT image. (a)Normal clinical *in-vivo* IV-OCT image. (b) Intensity-enhanced counterpart of (a). (Inset) shows enlarged view of the tissue2 and residual blood regions in (b). (c - e) Distribution of pixel intensities at selected regions, marked in (b). In all the plots the Gaussian fit was applied to the data. All regions except the blood flow region, exhibit a Gaussian distribution. The marking * indicates the guide-wire and its shadow artefact on the image.

and 4(b) respectively show a normal IV-OCT image and its lumen intensity-enhanced version. The image used here was also a representative model of challenges commonly observed in IV-OCT datasets. A lumen region, with residual blood circulation between the 6 and 5 'o' clock position but otherwise, with high-contrast was clearly identifiable in both Fig.4(a) and 4(b). A low-contrast lumen, of a side-branch, was also visible in both the images Fig.4(a) and 4(b). The image in Fig.4(b) was smoothed with a (2×2) averaging filter and then speckle analysis carried out for selected regions - lumen ($\square$),

tissue (tissue1☐, tissue2☐), low-contrast lumen (☐), background (☐) and residual blood artefact (☐) markedly shown in Fig.4(b). The histogram of pixel intensities at these regions demonstrated that all regions (see, Fig. 4(c) and 4(d)) except the residual blood flow region (see, Fig.4(e)) had a Gaussian distribution. From, Fig.4(c) it is also evident that the mean and SD values for the main and the low-contrast lumen regions were different when compared to their respective surrounding regions. It should be noted that speckle in OCT images are generally considered to have a Rayleigh type distribution.[15] This change in speckle distribution may be attributed to the interpolation method used for constructing such images from the polar-format counterpart.[16]

Statistics based segmentation method can also possibly discriminate lumen areas when the residual blood volume were very close and had similar intensities. This was demonstrated by the regions at 6 and 5 'o' clock position of Fig.4(a) and 4(b), where two sets of streaky structures - the outer blood flow and a tissue region jutting into the lumen are present. The speckle distribution at the residual blood flow region (see, Fig.4(e)) had a different type of distribution when compared to regions shown in Fig.4(c)) and 4(d).

2.2 *Localized region based level-set active contour method*

Application of the contrast enhancement technique, discussed in section 2.1, allowed direct visualization of the lumen and if the blood were effectively cleared, morphological operations would be adequate to extract the lumen shapes. However, in *in-vivo* clinical

IV-OCT images complete blood clearance is not always possible. The presence of blood in the lumen would reduce the transmissivity in those regions and therefore appear darker in the transmissivity maps. Thus images generated from these maps would also contain image artefacts for the luminal regions. In such cases, intensity dependent methods would require manual intervention to accurately extract the luminal boundaries. To overcome these issues and to automatically segment the lumen boundaries, a local region-based ACM method[17] with a level-set function was employed in this study. This segmentation approach followed the method proposed by Wang *et al.*[18] which had been demonstrated for medical images such as ultrasound and MR images but not implemented for IV-OCT datasets. Its essential derivation steps have been summarised in appendix A.

As it is an active contour based image segmentation method, an energy functional consisting of an image dependent data term and a length penalizing regularizer function that smooths the curve, was first defined. The image dependent energy functional was defined locally using the speckle distribution property of the image. As discussed in Sec. 2.1.1 and shown in Fig.4, Gaussian type speckle distribution was appropriate and therefore the level-set approach proposed by Wang[18] *et al.* was suitable. The image dependent energy functional term was defined for a local neighbourhood using the Gaussian probability distribution function shown in Eq. (5). The image dependent energy minimization term was derived on the basis that the contour segments the region so as to have a *maximum a pos-*
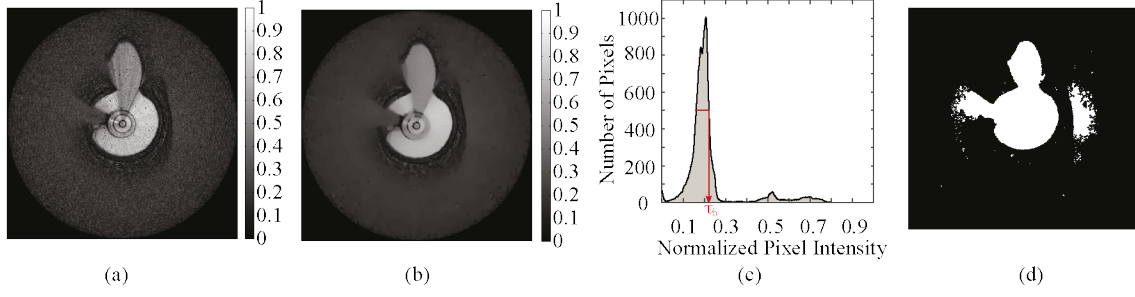
Fig 5 Initialization of the level-set function using image thresholding.(a) Lumen intensity-enhanced IV-OCT image. (b) Image smoothing using anisotropic diffusion scheme to reduce the speckle noise and to enhance the low SNR regions. (c) Histogram plot of pixel intensities of image in (b). The value at τ_h, was used as the threshold value. (d) Binary image of (b) obtained using the threshold value determined from the histogram.

teriori probability (MAP),[18] see Eq. (6). Since, it is a local-region based method, so this minimized energy term was localised by incorporating a window function into the energy equation, as shown in Eq. (8). Thus obtained local energy functional was integrated over the entire image region to obtain the energy functional term for the whole image.

The total energy functional employed in this study is shown in Eq. (12). It can be observed that this energy functional was also dependent on a level-set function, ϕ, which embedded the active contour as its zero level-set. Thus, ϕ provided an implicit representation of the evolving curve. The total energy functional in Eq. (12) was minimized to achieve the segmentation. The image dependent parameters, i.e., local mean (u_i) and standard deviation (σ_i) that minimized the energy functional are respectively shown in Eqs. (13) and (14). Finally using a gradient descent method, the equation (see, Eq. (15)) describing the curve evolution to minimize the energy, was determined.

The implementation of the local region based ACM method consisted of following

13

steps:

Step-1.1 - The initial level-set function ϕ_i for the lumen segmentation was derived from the image itself by taking a distance transform of the corresponding intensity thresholded binary image.

Step-1.2 - The the local mean, u_i and local SD, σ_i were respectively calculated using Eqs. (13) and (14) for a given ϕ_i. In both equations $\mathcal{W}$ was a kernel window of $(K \times K)$ size applied on to the image, I, for localization. The H_ε was determined using Eq.10 and subsequently used for determining $M_{i,\varepsilon}$.

Step-1.3 - The u_i and σ_i values were then used to solve the right hand side of Eq. (15). In Eq. (15) a suitable weighting constant, ν, value was used.

Step-1.4 - Using gradient descent method, Eq. (15) was solved to obtain a new level-set function,ϕ_{i+1}, i.e., $\phi_{i+1} = \phi_i + (\mathcal{E}\Delta t)$, where $\mathcal{E}$ represents the solution obtained in step - 1.3. Δt is the time-step.

Steps 1.1-1.4 were computed in a loop with N number of iterations, during which the contour was expected to trace the true lumen boundary. The parameters - kernel window size - K, weighting constant - ν, time-step - Δt and N were tuned to achieve accurate lumen segmentation. For implementing this segmentation method for a pullback dataset, these parametric values were generally determined for a selected frame and then applied

14

for every frame in the whole pullback dataset. If the segmentation was not fully achieved for any frames then the parametric values were altered and recomputed for the affected frames. For a pullback dataset the lumen segmentation was implemented sequentially for every frame in the stack. All the computational calculation involved in Steps 1.1-1.4 were performed in Matlab.

The binary image required for Step-1.1 was obtained by following the approach illustrated in Fig.5. The image was first smoothed using an edge preserving anisotropic diffusion[19] method (see, Fig.5(b)) and then from its histogram the upper value of the full-width at half maximum (FWHM) for the largest peak (see,Fig.5(c)) was determined. This value (τ_h in Fig.5(c)) was used as the threshold value to generate the binary image (as in Fig.5(d)). This process was performed automatically for every frame in the pullback. Additionally, morphological operations using bwareaopen, imfill and imclose functions of Matlab were performed on the binary images to respectively remove small isolated and to close holes if any present. These imperfections were found to increase the computation time for segmentation.

The ϕ_i of Step-1.1 was obtained by applying a Matlab function, bwdist - Euclidean distance transform function, to the binary mask (as in Fig.5(d)). The active contour was the zero level-set of the ϕ. Initial ϕ derived in this manner, ensured that the initial contour was in close proximity to the lumen boundary and therefore the lumen boundary can be
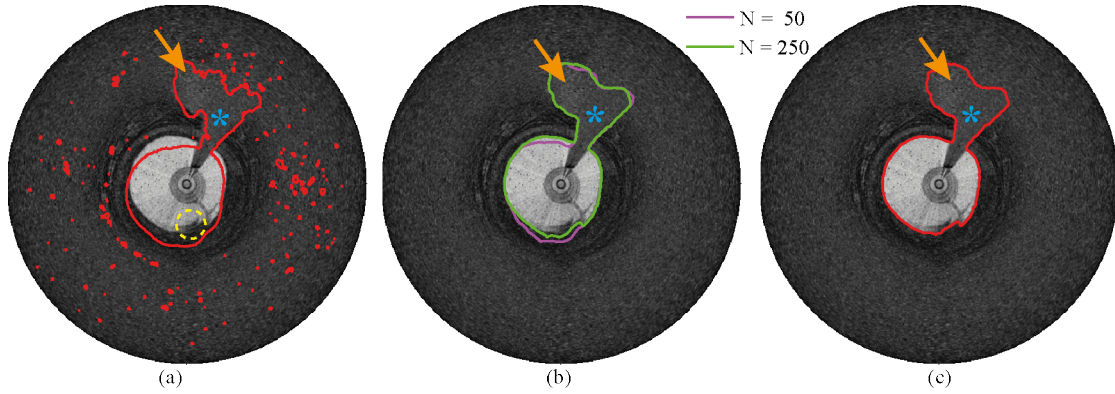
15

Fig 6 Local region based level-set based lumen segmentation method employing statistical properties of the image. (a) Initial contour at zero level-set of ϕ obtained from a binary image. (b) Intermediate zero level-set contours after N iterations. (c) Final zero level-set contour after 500 iterations. The encircled region in (a) highlights the lumen region which due to residual blood artefact appear as part of tissue region (darker area), however the final contour in (c) was able to segment the lumen correctly.The marking * indicates the guide-wire and the arrow points to the low-contrast region. The parametric values K $= 41$, N $= 500$, $\nu = 0.05 \times 255 \times 255$ and $\delta t = 0.01$ were used. The enlarged view of encircled region in (a) can be seen in the inset of Fig.4(b).

obtained very quickly. Because the initial contour was close to the lumen boundary so ϕ did not undergo large shape change as it evolved. Therefore no regularizer function, used by Wang[18] *et al.* to control the deviation in level-set function from its initial shape, was incorporated into the total energy functional in Eq. (12). The length penalizing regularizer function ($\mathcal{L}$) included in Eq. (12) controlled the smoothness of the contour.

Figure 6 demonstrates the lumen segmentation process, using a lumen intensity-enhanced IV-OCT image. The binary mask required for initializing ϕ was generated using the histogram approach shown in Fig.5. The ϕ_i obtained from a different binary mask was used to demonstrate the active contour evolution and segmentation of the lumen in the presence of artefact. Figure 6(a) shows the zero level-set of the ϕ_i overlayed on the top of the image to

be segmented. Small noisy contours that appear along with the larger contours, in Fig.6(a), were the artefacts in the binary mask. In actual implementation these small artefacts would be removed from the binary image through the morphological operations. As contour evolution progresses these noisy contours observed in Fig.6(a) disappears in Fig.6(b). N= 500 iterations were required to obtain the true lumen boundary. The final lumen contour in Fig.6(c) closely follows the lumen boundary. The lumen contour at the low-contrast region (marked by arrow in Fig.6(c)) also fitted its boundaries accurately. Though the lumen contour contained the guide-wire artefact (see, Fig.6(c)), this could be compensated by the method proposed in section 2.3. Curve evolution for the entire iteration, for Fig.6, can be seen in MOVIE1 file.

Though in Fig.6, N=500 iterations were employed, generally ≤ 50 iterations were required. This is because the ϕ_i were usually determined from the same image so the initial contour was close the actual lumen contour.

2.3 Guide-wire Correction using dynamic programming method

The guide-wire identification and its artefact correction is a requirement for segmentation of most *in-vivo* clinical IV-OCT images. In the Maximum Intensity Projection (MIP) of a polar-format, log-compressed IV-OCT image pullback stack the guide-wire appears as continuous feature[2,5](see, Fig.7(a). The guide-wire segmentation are usually achieved from the MIP images by means of intensity thresholding[2] or boundary detection through
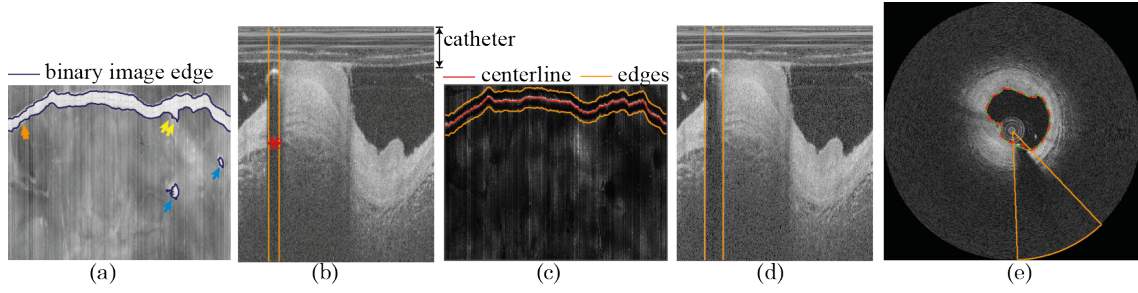
Fig 7 Illustration of the guide-wire segmentation approach. (a) Guide-wire segmentation by intensity thresholding of the maximum intensity projection (MIP) map of the pullback stack. The slim arrow points to the side-branches. bold arrow - guide-wire region underestimated, double arrow - side-branch misidentified as part of guide-wire. (b) Effect of underestimation of the guide-wire thickness. (c)Centerline contour obtained using dynamic programming method. Edge contours are the boundaries of the guide-wire obtained by shifting the centerline contour upwards and downwards by half the maximum width (i.e., 25 pixels) of the guide-wire. (d)Effect of underestimation of the guide-wire thickness. (e)The segment of the lumen contour (—) within the identified guide-wire area (—) was masked out and then interpolated over the region to obtain the final lumen contour (—) . The asterisks in (c) and (d) denote the guide-wire. The images in (b) and (d) had their background regions cropped out and enlarged for better view.

dynamic programming method.[5] As shown by the overlayed contour in Fig.7(a) some regions (marked by bold arrows) were missed out in intensity thresholding method. This would result in under-estimation of the guide-wire width as illustrated in Fig.7(b). While DP method may succeed in segmenting such guide-wire portions but it may fail to distinguish a guide-wire region from a side-branch if both were overlapping (see, double arrow area in Fig.7(a)). If the boundaries were indistinctive, accurate segmentation may not be possible and so require manual interference.

In this study the bright reflecting centreline (see, Fig.7(c)) of the guide-wire was segmented using a DP approach.[20] As a strongly reflective[1] body, it generally appears the brightest (metallic stents can also appear bright). From Fig.7(c), the optimal path,$P_{C_1 \longrightarrow C_N}$

18

for the guide-wire, starts from first column C_1 and trace up to the last column C_N. From all possible paths, the optimal path had the highest cumulative cost, with the cumulative cost, $G_{k,j}$, for a partial path $P_{C_i \longrightarrow C_j}$ defined as in Eq. (4).

$$G_{k,1} = I_{k,1}$$

$$G_{k,j} = I_{k,j} + \max_{k-n \leq k \leq k+n}\{G_{k,i}\} \quad \text{where, } 1 < j \leq N \text{ and } i < j$$

(4)

The $'I'$ in Eq. (4), represents the projection map (see, Fig.7(c)) from which the optimal path was determined. In Eq. (4), the subscripts (k, j) respectively refers to the rows and columns of the cumulative cost matrix, G. Since the optimal path had the highest cumulative cost, so the path retrieval process starts from the location for the highest cumulative value, i.e., $\max\{G_N\}$ - the maximum value in the last column of the G matrix. The process then retraces back through the preceding columns up to the first column, finding for every column the location (or, row) of the connected optimum predecessor , within the archived steps.

The index $'k \pm n'$ in Eq. (4), is the window length within which the path search was constrained. In this study $n = 10$, i.e., a window length of $(2n + 1) = 21$ was used for detecting the guide-wire. The red curve in Fig.7(c) traces the path detected by the DP based guide-wire detection method.

The width, d, of the guide-wire within a frame was assumed to be $d = d_{max}$, where d_{max} was the largest width observed in the pullback. Then two contours at distances of

19

($\frac{d}{2}$) from the detected guide-wire centerline were traced out on its either side, as shown in Fig.7(c). As each column of the map represents an IV-OCT image from a pullback dataset, so the radial co-ordinates for the two edges of the guide-wire artefact can be determined from the locations of the two outer contours at a given column. Once the guide-wire edge co-ordinates were determined, the lumen contour portions within it were masked out and the ends interpolated (as shown in Fig.7(e)).

Here it was assumed that every frame had the same width for the guide-wire artefact. However, in practise, narrowing and broadening of the guide-wire shadow are commonly observed in clinical datasets. Since, maximum width was considered, so in some frames the guide-wire artefact width would be over-estimated (see, Fig.7(d)). However, this had negligible effect on the final lumen contour as the lumen segment at the guide-wire shadow region and its vicinity were interpolated using curve shape information of much larger length.

2.4 Compensation of lumen contour at low-intensity segments of side branch

It was observed that sometimes the sections of the segmented lumen contour (from section-2.2) were inconsistent with the expected lumen shape. Such irregularities were especially observed for the side branch lumen segments that were either extending beyond the imaging range or had diffused boundaries. The presence of blood artefact further deteriorates the contrast of these regions. Also, sometimes parts of the side-branch would appear to
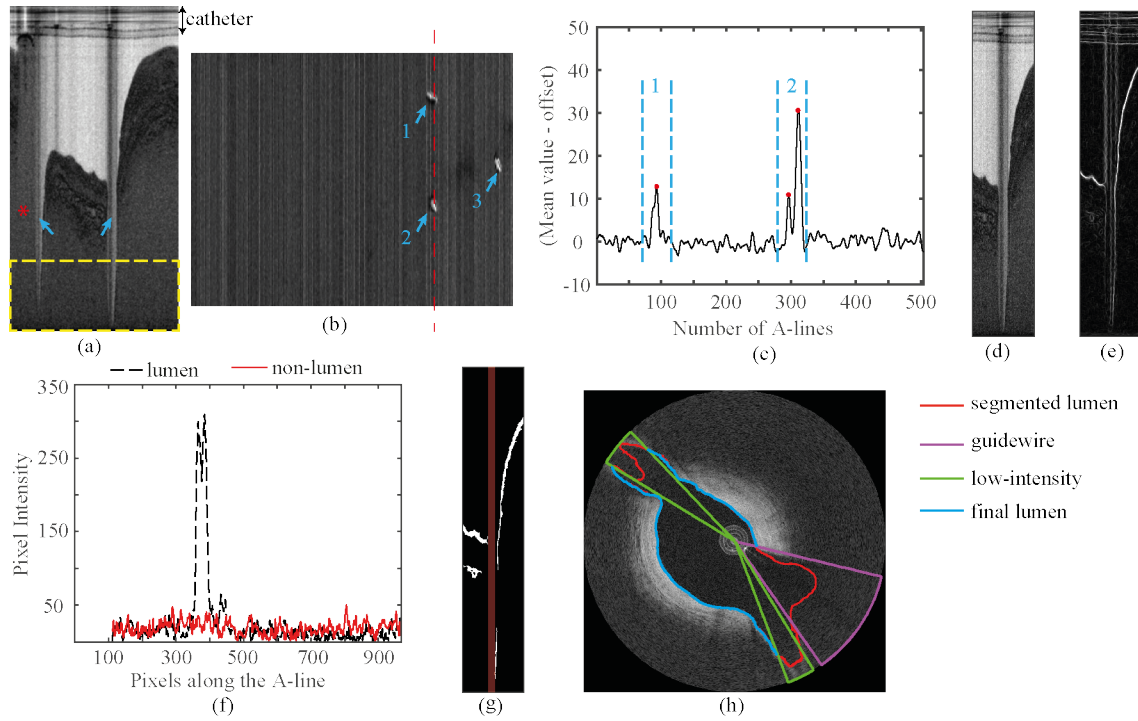
Fig 8 Compensation of the lumen contour discrepancy at low-intensity lumen boundaries of the side-branches. (a) Lumen intensity-enhanced IV-OCT image with side-branch regions (pointed arrows). (b) Mean intensity map for the last $N = 100$ rows (yellow dotted box in (a)) of every image in the pullback stack. The side-branches (numbered) are conspicuous. (c) Line profile of the values along the dotted line in (b) for the image in (a). (d)Using the side branch location information in (b) 2nd side branch in (a) was segregated. (e) Image gradient operation applied to (d) for identifying low intensity lumen regions of the side branch. Only true lumen boundaries had strong gradient. (f) Comparison of true lumen and noisy regions in the gradient image. (g) Intensity thresholded binary image of (e). The catheter region has been masked out. Only the lumen regions that had a strong gradient are observed in the binary image. The empty A-lines (shaded red) between these regions were identified as low-contrast regions, as highlighted by the overlay plot in (g). (h) The low-intensity lumen regions of the side-branches in (a) were thus identified and the lumen contour within these regions was masked out to obtain the final lumen.The asterisk in (a) denotes the guide-wire.

fold over into the image due to limitations in the ranging depth.[10] In such scenarios lumen segmentation methods cannot guarantee accurate lumen contour for the affected regions. Corrupted lumen contours can affect the lumen quantification methods such as geometri-

21

cal analysis[3,4] of contour to identify bifurcation points of the side branches. To overcome it a scheme is presented wherein low-intensity lumen regions of the side branches were identified and subsequently the erroneous contour sections were masked out.

The implementation of the compensation method consisted of following steps:

Step-2.1 - An intensity map was first constructed using the mean intensity for the last $'N'$ rows of the polar-format lumen intensity-enhanced IV-OCT images in the pullback.

Step-2.2 - By intensity thresholding, the side-branch location within a frame and the frame number were automatically identified from the intensity map.

Step-2.3 - Using the location information from Step-2.2 the side-branch and its surrounding regions were selected from the frame and then sobel-type image gradient was applied.

Step-2.4 - By intensity thresholding low gradient regions were suppressed and a binary image containing only strong lumen boundaries was constructed.

Step-2.5 - The empty A-lines of the binary image that had strong lumen gradient regions on its either side were automatically identified as regions requiring contour compensation.

The implementation of the method is illustrated in Fig.8. As shown in Fig.8(b), the locations of the side-branches within a pullback can be easily visualized through Step-2.1. High contrast was achieved for side-branch regions, as shown in Fig.8(c). This was possible because the lumen intensity enhancement (see, section 2.1) enabled lumen regions

of the side-branches to have higher intensity than its surrounding regions, especially when the side branches extended beyond the ranging depth (as in Fig.8(a)). The intensity thresholding in Step-2.2 was applied and a binary image containing only the side branches was constructed. From this binary image the frames containing the side-branches can be easily identified.

The determination of the extent of the side-branch, within a frame, was achieved by identifying the corresponding peak (as in Fig.8(c)) and then averaging the values of the twenty sample points on either side of the peak. The A-lines within the selected peak region which had this average value was considered as the span of that particular side branch. It can be noticed that this was a rough estimate, as it depended upon the $'N'$ value used to generate the mean intensity map (e.g., Fig.8(b)) and also on accurate determination of the peak positions. However, the rough estimate of the side branch location was adequate for determining the low-contrast lumen regions of the side branch. From Fig.8(c) the width of the side-branches in Fig.8(a) were determined in terms of A-lines.

The implementation of Step-2.3 for Fig.8(a) is shown in Fig.8(d) and 8(e). The image gradient operation enhanced the lumen regions with strong boundaries while low-contrast regions appeared noisy (see, Fig.8(e)) and further illustrated in Fig.8(f). Before, Step-2.4 was applied the strong gradient locations of the catheter were masked out. Accurate knowledge of the catheter boundaries were not necessary as the lumen region of the se-

lected side-branch was always away from the catheter. In the case of Fig.8(e) all the rows ≤ 100 were masked out.

The binary image obtained for Fig.8(e), from Step-2.4, contained only lumen regions with strong boundaries (see, Fig.8(g)). This was achieved by applying a unique threshold value for every A-line in the gradient image. The threshold value,th, for a given A-line was defined as the sum of the mean (M) and twice the standard deviations(SD) (i.e., $th = M + 2 \times SD$) of the gradient profile. Any gradient value below the threshold was assumed to be noise and therefore suppressed. Subsequently a binary image containing only the strong lumen boundaries was generated. Sometimes, localized blood artefacts may appear in the binary image but due to their relatively smaller size were removed by morphological operations such as bwareaopen and imclose Matlab functions. Using Step-2.5 the span of the low-contrast lumen regions were determined from he binary image.

The lumen contour (from section 2.2) was then corrected by masking out the contour sections over the low-contrast regions. The contour correction of the IV-OCT in Fig.8 is shown in Fig.8(h) where both the initial uncorrected and the final contour has been displayed. Also the low-contrast segments obtained by this method has been overlayed alongside the detected guide-wire segment (from section 2.3).

Table 1 Computational time required for each of the image processing methods on a HP EliteBook laptop.

Method	Image Size	Computing time (sec)
Transmissivity mapping	968×504	1.15
Polar-Image transform	968×504	2.89
Edge preserved smoothing	512×512	4.3
Lumen segmentation (20 iteration)	512×512	< 4
Guide-wire	504×270	0.47
Low-contrast side-branch	$968 \times 504 \times 270$	47.54

2.5 Computational Implementation

The image processing methods - lumen enhancement, followed by its segmentation and contour correction for artefacts, was implemented in Matlab 2015a, 64-bit version-8.5 (MathWorks, Natick, MA). The programs were first applied on a HP EliteBook 8770w laptop (Intel Core i7-3720QM, 32GB RAM and 64 bit Windows 7). The computational time required for each method is listed in Table.1. On a per frame basis, the largest computing time was required for the anisotropic diffusion based edge preserved smoothing. Whereas, the guide-wire segmentation from the projection image of a pullback dataset required only 0.47 seconds to compute.

Computational analysis for the validation studies (discussed in section 4) were however performed on the High Performance Computing (HPC) facility of the University of Leicester, UK. The computing jobs were submitted as serial jobs and allocated only 1 node and 1 processor core with 8 gigabyte(GB) memory. The HPC system accepted all the job submission for validation study and serially computed every dataset at the same time. This greatly saved the total computational time.

3 Materials

A St Jude C7-XR IV-OCT (St Jude inc., USA, "ILUMIEN^{TM}") clinical system was used for all imaging. This system has a fixed A-scan rate of 50 kHz and frame-rate of 100 Hz. All the imaging was performed with a pullback speed of 20 mm/sec and travel length of 54 mm. Each circumferential scan consists of 504 A-lines, which were then transformed into polar form as cross-sectional images. A clinical grade catheter (C7 Dragonfly, St Jude inc., USA, "ILUMIEN^{TM}") was used throughout the study. The lumen intensity enhancement and the segmentation was further applied to an anonymised clinical IV-OCT dataset. Imaging was performed after contrast flushing for blood clearance. Human imaging was undertaken on clinical grounds as part of procedures undertaken with informed consent according to institutional guidelines for the University Hosptials of Leicester, UK.

4 Validation Experiments

The image processing approach presented in section 2 was applied to 30 randomly selected clinical IV-OCT pullback dataset and then compared with manual segmentation, performed by two independent image analysis experts. The first observer, O1, manually analyzed every 20th frame in each of the 30 datasets, while the second observer, O2, performed the same for first 15 datasets. Each pullback dataset consisted of 270 frames. The selected datasets contained images corrupted by blood artifacts and catheter rotation

issues. Four pullback dataset had last 20 - 40 frames completely lost to blood circulation. Six dataset contained metallic stents while 3 dataset had bioreabsorbable vascular scaffolds (BVS); rest of the dataset did not have any stent or scaffolds. All 30 datasets contained the guide-wire artifact.

Both O1 and O2 observers manually segmented the lumen region using the roipoly Matlab function. The lumen contour was then generated as an outline for the segmented region. For manual segmentation normal IV-OCT images (like, Fig.7(h)) were used, while the computed approach used the lumen intensity-enhanced IV-OCT images, as in Fig.6. The degree of agreement between any two segmentations, i.e O1 vs O2, O1 vs At and O2 vs At (where, At refers to automatic method), were carried out using intra-class coefficient (ICC) method.[4] For any two segmentations, the ICC method compared the radial distance (measured in pixels) of the lumen contour points from the image centre. The radial distance error (i.e., differences in the measured radial distance) between any two approaches were also performed. The interpolated lumen segment for the guide-wire artefact, were not considered for the comparison.

For the manual analysis of the guide-wire, polar-format images (e.g., Fig.7(b)) were used and both observers visually determined the radial distance (measured in pixels) of the bright centre location from the top of the image. Thus identified guide-wire distance (by O1 and O2 observers) and also extracted automatically (section 2.3) were compared using
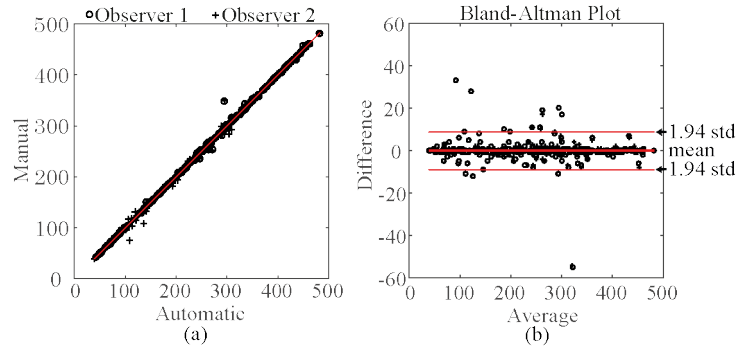
27

Fig 9 Validating the guide-wire segmentation. (a) Comparison of manual and automatic guide-wire segmentation results. The A-line position of the guide-wire center determined by respective methods were compared. A strong linear correlation can be observed. (b) Bland-Altman plot compares the differences between each observer vs the automatic method.

the ICC and Bland-Altman methods.

To validate the automatic method presented in section 2.4, both manual observers O1 and O2 only analysed the side-branches with low-contrast lumen, out of the 81 side branches that were present in the 30 datasets. O1 observer analyzed 28 side branches while its subset of 18 side branches were evaluated by the observer O2. Polar-format log-scale compressed normal IV-OCT images were used and the angular width and location of the signal-sparse lumen regions of the side-branches were determined in terms of the A-line separations.

5 Results

The ICC comparison of the automated lumen segmentation with both manual segmentations exhibited a high correlation, as O1 vs At and O2 vs At respectively had 0.912 and 0.893 correlation values. Difference in the radial distances between the computed and

Table 2 Comparison of the manual (O1 and O2) and automatic (At) methods for segmentation of lumen and guide-wire and identification of low-contrast regions in side branches.

		O1 vs At	O2 vs At	O1 vs O2
Lumen	ICC	0.912	0.893	0.999
	Diff	-1.815 ± 18.6037	-1.4258 ± 18.793	-0.521 ± 1.339
Guide-wire	ICC	0.999	0.999	1.0
	BA	-0.1569 ± 8.9951	-0.0725 ± 8.9792	-0.3478 ± 2.215
Side branch	TP (%)	60	59	75
	FP (%)	13	13.5	8.75
	Dice	0.78 ± 0.2	0.78 ± 0.2	0.87 ± 0.14

manually segmented lumens showed an average error of -1.82 ± 18.6 and -1.43 ± 18.8. As expected both manual segmentations closely matched each other and the radial distance error was about -0.5 ± 1.3.

Automatic vs manual segmentation analysis of the guide-wire centerline also showed a high correlation, as shown in Fig. 9. In Fig. 9(a) manual observations are plotted against the automatic measurement and a strong linear relationship was observed. The Bland-Altman (BA) plot, in Fig. 9(b), compares each observer (O1 and O2) against the automatic method and shows a narrow spread for both cases. A mean bias of $\sim -0.16 \pm 9$ and $\sim -0.07 \pm 9$ was respectively obtained with respect to observers O1 and O2.

The contour correction approach (in section 2.4) was validated with manual observations (by O1 and O2 observers), which detected the signal sparse lumen boundaries at the side-branches, where lumen segmentation approach would possibly fail. Between the two observers O1 and O2, 75% (true positive rate - TP value) of the 18 side-branches, which had the degraded lumen segments were detected correctly and with 8.75% false positives

(FP). Comparison of the observer against the automatic approach shows that 60% of the 28 (O1 observer) and 18 (O2 observer) side-branches with such lumen segments, can be correctly identified and with about 13.5% FP. The average Dice's coefficient for the angular spread of the detected signal sparse side branch lumen region versus the two observers' measurement were about 0.78 ± 0.2. Comparatively lower TP values were observed here because the low (signal-to-noise ratio) SNR pixel intensities at these regions resulted in variation of the boundary locations, determined by each method. Since this approach is employed only to mask out the corrupted lumen contour segments so such TP values were adequate.

A summary of the results for validation of lumen and guide-wire segmentations and automatic identification of low contrast lumen regions of the side branches have been presented in Table 2.

6 Additional Capabilities

The intensities of all luminal regions can be enhanced by the transmittance mapping method (section 2.1). With the proposed level-set based lumen segmentation method multiple lumens can therefore be simultaneously segmented, as shown in Fig.10)(a). The steps illustrated in Fig.2 and described in section 2.2 were followed for this segmentation. It can be noticed that all the larger lumens and smaller microvascular lumens (at 11 and 12 'o' clock position in Fig.10(a)) were segmented by this approach. Common lumen segmenta-
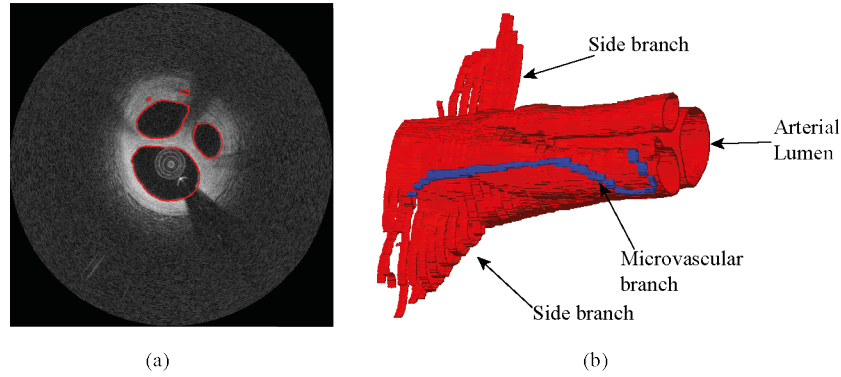
Fig 10 Segmentation of multiple lumen using the proposed method. (a)Lumen shapes of various sizes have been simultaneously segmented using the proposed method. (b)3D visualization of the lumen geometry.

tion methods,[1,2,4] have generally been shown for single simple lumen geometries. Whilst observation of multiple lumens (as in Fig.10(a)) may not be common, lumen dissections are not uncommonly observed in coronary artery diseases.[10,21] It can also be shown that the proposed method can also extract elements of the plaque associated microvasculature, a prevalent feature related to atherosclerotic plaque progression.[22,23] By applying the proposed segmentation approach to a pullback it was possible to not only construct a 3D vessel geometry but also visualize the microvascular branch associated with the main artery (see, Fig.10(b)).

7 Comparison of the proposed segmentation methods with other methods

The performance of the proposed segmentation method was compared with another contour evolution approach - Chan-Vese[24](CV) method and manual segmentation. The CV method has been employed for IV-OCT image segmentation,[1] whereas manual segmenta-
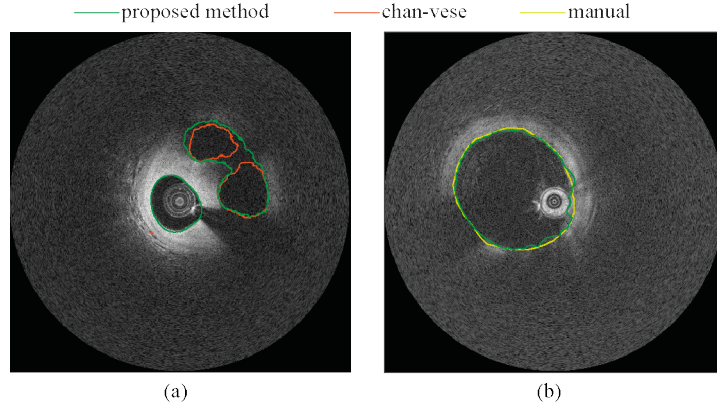
Fig 11 Comparison of the proposed lumen segmentation with chan-vese (CV) and manual segmentation methods. (a) Multiple lumens segmented by the current approach and CV technique. Same initial ϕ was used in both cases. Contour for the CV method continued to evolve past the lumen boundaries until the iteration stopped while in the proposed the contour stopped to evolve at the true lumen. (b) Low-contrast lumen image segmented by both manual and localized level-set methods. Though both contours closely follow the same path, the manually obtained lumen is very smooth.

tion is still a gold standard for lumen segmentation and commonly used for validating (as in section 4) the techniques.

The CV method and local region-based ACM (section 2.2) were applied to an IV-OCT image containing multiple lumen. The same initial ϕ, derived from a particular binary mask was used in both cases. The final lumen contour generated by both approaches are shown in Fig.11(a). The evolution of the local region based contour stopped once it had arrived at the lumen boundary however the CV based active contour progressed till the iteration stopped. The full evolution of both contours during the iteration can be seen in MOVIE2 file. Thus global region based techniques such as CV method have limitations when the contrast are low.

Though a quantitative comparison of manual and the proposed segmentation approach

has been provided in section 4, a visual comparison of both techniques is done in Fig.11(b). It can be observed that the automated method was able to generate a closely resembling lumen contour even though the contrast of the arterial cross-section was poor. Certain discrepancies can be noticed, where the automated contour appear not to be as smooth as the manual contour. This may be due to the diffused boundaries of the low-contrast lumen.

8 Discussion

In this study, a lumen segmentation method was presented that can not only extract the lumen boundaries automatically from a 3D image-stack but also handle blood artifact and correct the contour for the guide-wire artefacts and side-branches. Generally, a sequential approach is followed for lumen segmentation, where, first the catheter, its covering sheath and guide-wire are removed from the image and then the lumen is segmented.[4] No such steps were required in the proposed method, as lumen intensity-enhanced IV-OCT images were used for segmenting the lumen boundaries. This was possible as a result of the large transmissivity (see, Sec.2.1) in the luminal region, which created a contrast between the lumen and its surrounding tissue and background regions.

Pullback datasets that provided various image processing challenges - shadowing effects, presence of residual blood, multiple lumen, low-contrast regions and microvascular features were used in this current study. The ability of the proposed segmentation method to segment the lumen in presence of these challenges proved the capability of the tech-

33

nique. Generally the lumen segmentation method was implemented directly for a pullback stack using the $\nu, \Delta t$, K and N values determined for one of the frames in the stack. No human intervention was required when the true lumen boundary was the only one nearest to the zero level-set contour of ϕ. Sometimes when the contour was close to the ablumi-nal borders of a plaque it could evolve towards this boundary than the true lumen. This was due to the threshold level used in Step-1.1, whereby non-luminal regions were also be included in the ϕ_i. In such cases, the threshold level was modified and the lumen seg-mentation process (steps in section 2.2) was repeated for those frames. In some images blood-flow artefacts such as a blood column linking the lumen and the catheter or flow-ing very close to the wall, etc. could influence the contour evolution. In such cases the parametric values were tuned so that true lumen were segmented quickly. As shown in Fig.11(b) sometimes lumen regions associated with the lumen may have low contrast and depending upon the parametric values the contours may not be very smooth. In such cases by tuning the parametric values desired lumen smoothness can be achieved. However, during validation analysis no such corrections were performed during lumen segmenta-tion. Thus, the ICC and Diff values for lumen segmentation in Table.2 can be further improved by using specific parametric values for affected frames.

The contour compensation method discussed in section 2.4 were applied only to mask out abnormal contour sections resulting from the degraded lumen boundaries at far re-

gions of the side-branch. The masked out sections can be interpolated as performed for the guide-wire. However, in Fig.8(h) this was not preformed because at the first side-branch there was an overlapping guide-wire shadow, while the second side-branch extended beyond the imaging range.

In the present study all the computing was performed serially in a Matlab environment. This increased the computational time as observed in Table.1. The processing times for Polar-Image conversion and anisotropy based edge preserved image smoothing methods can be greatly reduced when performed in C or C++. The lumen segmentation method can be made 15 times faster by making the job parallel and implementing it some graphical processing units (GPUs).[25]

While level-set based localized region ACM was used in this study, alternate approaches such as MRF[7] or EM[8] labelling method could also be applied to lumen intensity-enhanced IV-OCT images, to segment the lumen. The advantage of using lumen intensity-enhanced images are that labelling technique can now cluster the lumen regions separately from the background regions, which was not possible in non-enhanced IV-OCT images. Thus, this transmissivity based lumen intensity enhancement method allows direct segmentation of the lumen, instead of inferring it from the tissue boundaries.

As improved IV-OCT systems are made clinically available and with high-density volume imaging,[26] it would be possible to construct microvascular beds associated with

35

atherosclerosis, in *in-vivo* clinical cases. While, this lumen segmentation method can identify blood-cleared microvessels, cross-correlation based microvessel segmentation[22, 23] can be used to extract other microvessels with blood flow in it. Both approaches when put together can help in visualizing the complete microvasculature.

9 Conclusions

An automatic lumen segmentation approach for IV-OCT pullback dataset was demonstrated, which combines the transmissivity property of luminal regions and the capability of the localized level-set segmentation method to extract luminal boundaries. Transmissivity based mapping method enhanced the lumen intensity while the localized level-set method employed local speckle distribution properties to evolve the zero-level set function towards the object boundary. The technique performed adequately even in the presence of image artefacts such as loss of contrast and presence of residual blood. The proposed segmentation tool also performs correction for guide-wire artefact and accurately demonstrates side-branch openings.

Appendix A: Derivation of localized gaussian speckle distribution based level-set ACM method

The energy functional is derived on the assumption that the intensity-enhanced IV-OCT image have Gaussian type speckle distribution, as shown in Eq. (5)

$$p(I) = \frac{1}{\sqrt{2\pi}\sigma} \exp\left(-\frac{(u-I)^2}{2\sigma^2}\right) \tag{5}$$

where, σ and u denotes the standard deviation (SD) and mean of the pixel intensities at the selected region of the image.

As shown by Wang[18] *et al.*, for any given local region $\mathcal{O}_x$ to be segmented on the basis of MAP, requires that the product of the probability distribution in each sub-region, namely $\mathcal{O}_x \cap \Omega_1$ and $\mathcal{O}_x \cap \Omega_2$, should be a maxima, (i.e., $\prod_{i=1}^{2} \prod_{y \in \mathcal{O}_x \cap \Omega_i} p_{i,x}(I(y))$ is maximum, where $p_{i,x}(I(y))$ follows Eq.(5)). By taking a log of this term and introducing a minus sign, so that the energy is minimized, the image dependent energy functional is defined. Thus, the energy minimization term for the localized region $\mathcal{O}_x$, is expressed as

$$E_x = \sum_{i=1}^{2} \int_{\mathcal{O}_X \cap \Omega_i} -\log p_{i,x}(I(y)) dy \tag{6}$$

Equation (6) can be generalized for any local region by defining a window function that can be introduced at any location of the image. Any region outside the window function will be masked out. $\mathcal{W}$ is the window function used in the current study and is expressed

37

as

$$W(x, y) = \begin{cases} 1, & \|x - y\| < r \\ \\ 0, & \text{otherwise.} \end{cases} \tag{7}$$

where, r is the radius parameter of the window

Thus Eq. (6) can be expressed as

$$E_x = \sum_{i=1}^{2} \int_{\Omega_i} -W(x - y) \log p_{i,x}(I(y)) dy \tag{8}$$

As shown in Eq.(8), the W is centered at the point x in the image. By integrating Eq.(8) over the entire image domain, $E = \int_\Omega E_x dx$, the energy functional for the whole image can be obtained.

In this study, the closed contour C is considered to be the zero level-set of an implicit level-set function, ϕ, (i.e., contour, $C = \{\mathbf{x} : \phi(\mathbf{x}) = 0\}$). Thus for a given local region $\mathcal{O}_x$, the two regions Ω_1 and Ω_2 can be defined in terms of ϕ as $\Omega_1 = \{\mathbf{x} : \phi(\mathbf{x}) > 0\}$ and $\Omega_2 = \{\mathbf{x} : \phi(\mathbf{x}) < 0\}$. As both are disjoint regions, so when Heaviside function is applied to ϕ, each region can be identified. Thus rewriting Eq.(8) in terms of ϕ and the Heaviside function gives

$$E_x = -\int W(x - y) \Big(\log p_{1,x}(I(y)) H_\varepsilon(\phi(y)) + \log p_{2,x}(I(y)) \big[1 - H_\varepsilon(\phi(y)) \big] \Big) dy \tag{9}$$

For computational implementation, in the Eq.9 a smoothed Heaviside function, H_ε is

38

used and it is defined as

$$H_\varepsilon(x) = \frac{1}{2}\left[1 + \frac{2}{\pi}\arctan\left(\frac{x}{\varepsilon}\right)\right] \tag{10}$$

and its derivative δ_ε is defined as follows

$$\delta_\varepsilon(x) = H'_\varepsilon(x) = \frac{1}{\pi}\frac{\varepsilon}{\varepsilon^2 + x^2} \tag{11}$$

By integrating Eq.(9) for entire image domain, the energy E as a function of ϕ can be obtained. Generally, in level-set ACM methods a regularizing function, $\mathcal{L}$, that smooths the contour by penalizing its length, is added to the energy functional. Thus the total energy functional is expressed as

$$\mathcal{F} = \int_\Omega E_x dx + \nu\mathcal{L}(\phi)$$

$$= \int_\Omega -\int \mathcal{W}(x - y)\left(\log p_{1,x}(I(y))H_\varepsilon(\phi(y)) + \log p_{2,x}(I(y))\left[1 - H_\varepsilon(\phi(y))\right]\right)dy dx$$

$$+ \nu\int |\nabla H(\phi(x))|dx$$

$$\tag{12}$$

where $\nu > 0$ is the weighting constant.

For segmentation this energy functional in Eq. (12) should be minimized. It can be noted that this energy functional is not only a function of ϕ but also of mean, u_i, and SD , σ_i, values for each ith region, as a result of the probability function, $p_{i,x}$, in the equation. Therefore to minimize the functional, in terms of its parameters $u_1, u_2, \sigma_1, \sigma_2$, calculus of variation is used.[18] The expression for these parameters at which the energy is minimised,

can be obtained by applying Euler-Lagrange equation[18] to Eq. (12) and is summarised here.

$$u_i(x) = \frac{\int \mathcal{W}(y-x)I(y)M_{i,\varepsilon}(\phi(y))dy}{\int \mathcal{W}(y-x)M_{i,\varepsilon}(\phi(y))dy} \tag{13}$$

$$\sigma_i(x)^2 = \frac{\int \mathcal{W}(y-x)(u_i(x)-I(y))^2 M_{i,\varepsilon}(\phi(y))dy}{\int \mathcal{W}(y-x)M_{i,\varepsilon}(\phi(y))dy} \tag{14}$$

In Eqs. (13) and (14) $i = 1, 2$; $M_{1,\varepsilon}(\phi(y)) = H_\varepsilon(\phi(y))$ and $M_{2,\varepsilon}(\phi(y)) = \big(1 - H_\varepsilon(\phi(y))\big)$. Finally the energy functional in Eq. (12) is minimized in terms of ϕ, using gradient descent method,[18] which gives the following gradient flow equation

$$\frac{\partial \phi}{\partial t} = \delta(\phi) \int \mathcal{W}(y-x)\left(\log\left(\frac{\sigma_1(y)}{\sigma_2(y)}\right) + \frac{(u_1(y)-I(x))^2}{2\sigma_1(y)^2} - \frac{(u_2(y)-I(x))^2}{2\sigma_2(y)^2} \right)dy$$
$$+ \nu\delta(\phi)\, \mathrm{div}\left(\frac{\nabla\phi}{|\nabla\phi|}\right)$$

$$\tag{15}$$

References

1 Z. Wang, H. Kyono, H. G. Bezerra, H. Wang, M. Gargesha, C. Alraies, C. Xu, J. M. Schmitt, D. L. Wilson, M. A. Costa, and A. M. Rollins, "Semiautomatic segmentation and quantification of calcified plaques in intracoronary optical coherence tomography images," *Journal of Biomedical Optics* **15**, 061711 (2010). [doi:10.1117/1.3506212].

2 G. J. Ughi, T. Adriaenssens, W. Desmet, and J. Dhooge, "Fully automatic three-dimensional visualization of intravascular optical coherence tomography images: methods and feasibility in vivo," *Biomed. Opt. Express* **3**, 3291–3303 (2012). [doi: 10.1364/BOE.3.003291].

3 M. M. G. Macedo, W. V. N. Guimarães, M. Z. Galon, C. K. Takimura, P. A. Lemos, and M. A. Gutierrez, "A bifurcation identifier for iv-oct using orthogonal least squares and supervised machine learning," *Computerized Medical Imaging and Graphics* **46**, 237–248 (2015). [doi: 10.1016/j.compmedimag.2015.09.004].

4 A. Wang, J. Eggermont, J. H. C. Reiber, and J. Dijkstra, "Fully automated side branch detection in intravascular optical coherence tomography pullback runs," *Biomed. Opt. Express* **5**, 3160–3173 (2014). [doi: 10.1364/BOE.5.003160].

5 Z. Wang, D. Chamie, H. G. Bezerra, H. Yamamoto, J. Kanovsky, D. L. Wilson, M. A. Costa, and A. M. Rollins, "Volumetric quantification of fibrous caps using

intravascular optical coherence tomography," *Biomed. Opt. Express* **3**, 1413–1426 (2012). [doi: 10.1364/BOE.3.001413].

6 G. Unal, S. Gurmeric, and S. G. Carlier, "Stent implant follow-up in intravascular optical coherence tomography images," *Int. J. Cardiovasc. Imaging* **26**, 809–816 (2010). [doi: 10.1007/s10554-009-9508-4].

7 S. Tsantis, G. C. Kagadis, K. Katsanos, D. Karnabatidis, G. Bourantas, and G. C. Nikiforidis, "Automatic vessel lumen segmentation and stent strut detection in intravascular optical coherence tomography," *Med. physics* **39**, 503–513 (2012). [doi: 10.1118/1.3673067].

8 K. Tung, W. Shi, R. D. Silva, E. Edwards, and D. Rueckert, "Automatical vessel wall detection in intravascular coronary oct," in *Biomedical Imaging: From Nano to Macro, 2011 IEEE International Symposium on*, 610–613 (2011). [doi:10.1109/ISBI.2011.5872481].

9 G. J. Ughi, T. Adriaenssens, P. Sinnaeve, W. Desmet, and J. Dhooge, "Automated tissue characterization of in vivo atherosclerotic plaques by intravascular optical coherence tomography images," *Biomed. Opt. Express* **4**, 1014–1030 (2013). [doi: 10.1364/BOE.4.001014].

10 G. J. Tearney, E. Regar, T. Akasaka, T. Adriaenssens, P. Barlis, H. G. Bezerra, and B. B. *et al.*, "Consensus standards for acquisition, measurement, and reporting of

intravascular optical coherence tomography studies: a report from the international working group for intravascular optical coherence tomography standardization and validation," *Journal of the American College of Cardiology* **59**, 1058–1072 (2012). [doi:10.1016/j.jacc.2011.09.079].

11 M. J. A. Girard, N. G. Strouthidis, C. R. Ethier, and J. M. Mari, "Shadow removal and contrast enhancement in optical coherence tomography images of the human optic nerve head," *Invest Ophthalmol Vis Sci* **52**, 7738–7748 (2011). [doi: 10.1167/iovs.10-6925].

12 K. Vermeer, J. Mo, J. Weda, H. Lemij, and J. de Boer, "Depth-resolved model-based reconstruction of attenuation coefficients in optical coherence tomography," *Biomed. Opt. Express* **5**, 322–337 (2014). [doi: 10.1364/BOE.5.000322].

13 C. Xu, J. M. Schmitt, S. G. Carlier, and R. Virmani, "Characterization of atherosclerosis plaques by measuring both backscattering and attenuation coefficients in optical coherence tomography," *Journal of Biomedical Optics* **13**, 034003 (2008). [doi:10.1117/1.2927464].

14 G. van Soest, T. Goderie, E. Regar, S. Koljenovic, G. L. J. H. van Leenders, N. Gonzalo, S. van Noorden, T. Okamura, B. E. Bouma, G. J. Tearney, J. W. Oosterhuis, P. W. Serruys, and A. F. W. van der Steen, "Atherosclerotic tissue characterization in

vivo by optical coherence tomography attenuation imaging," *Journal of Biomedical Optics* **15**, 011105 (2010). [doi:10.1117/1.3280271].

15 M. Pircher, E. Gotzinger, R. Leitgeb, A. F. Fercher, and C. K. Hitzenberger, "Speckle reduction in optical coherence tomography by frequency compunding," *Journal of Biomedical Optics* **8**, 565–569 (2003). [doi:10.1117/1.1578087].

16 G. Vegas-Snchez-Ferrero, M. Martn-Fernndez, and J. M. Sanches, "A gamma mixture model for ivus imaging," in *Multi-Modality Atherosclerosis Imaging and Diagnosis*, L. Saba, J. M. Sanches, L. M. Pedro, and J. S. Suri, Eds., 155–171, Springer New York (2014).

17 S. Lankton and A. Tannenbaum, "Localizing region-based active contours," *IEEE Trans. Image Proc.* **17**, 2029–2039 (2008). [doi:10.1109/TIP.2008.2004611].

18 L. Wang, L. He, A. Mishra, and C. Li, "Active contours driven by local gaussian distribution fitting energy," *Signal Processing* **89**, 2435–2447 (2009). [doi:10.1016/j.sigpro.2009.03.014].

19 S. Aja-Fernndez and C. Alberola-Lpez, "On the estimation of the coefficient of variation for anisotropic diffusion speckle filtering," *IEEE Trans. Image Proc.* **15**, 2694–2701 (2006). [doi:10.1109/TIP.2006.877360].

20 G. van Soest, J. G. Bosch, and A. F. W. van der Steen, "Azimuthal registration of

image sequences affected by nonuniform rotation distortion," *IEEE Trans Inf Technol Biomed* **12**, 348–355 (2008). [doi:10.1109/TITB.2007.908000].

21 N. S. van Ditzhuijzen, J. Ligthart, S. Tu, M. van der Linden, and E. Regar, "Optical coherence tomography-guided bifurcation stenting of a coronary artery dissection," *Canadian Journal of Cardiology* **30**, 956.e11–956.e14 (2014). [doi:10.1016/j.cjca.2014.04.009].

22 S. Joseph, C. Rousseau, H. M. Subhash, M. J. Leahy, and D. Adlam, "Variation in cross-correlation as a discriminator for microvessel imaging using clinical intravascular optical coherence tomography systems," in *Optical Coherence Tomography and Coherence Domain Optical Methods in Biomedicine XVIII*, J. G. Fujimoto, J. A. Izatt, and V. V. Tuchin, Eds., *Proc. SPIE* **8934**, 89342L1–89342L7 (2014). [doi: 10.1117/12.2042053].

23 S. Joseph, A. Adnan, H. M. Subhash, M. Leahy, and D. Adlam, "Developing cross-correlation as a method for microvessel imaging using clinical intravascular optical coherence tomography systems," *Biomed. Opt. Express* **6**, 668–689 (2015). [doi: 10.1364/BOE.6.000668].

24 T. Chan and L. Vese, "Active contours without edges," *IEEE Trans. Image Proc.* **10**, 266–277 (2001). [doi: 10.1109/83.902291].

25 E. Smistad, T. L. Falch, M. Bozorgi, A. C. Elster, and F. Lindseth, "Medical image

segmentation on gpus a comprehensive review," *Medical Image Analysis* **20**, 1–18 (2015). [doi: 10.1016/j.media.2014.10.012].

26 T. Wang, T. Pfeiffer, E. Regar, W. Wieser, H. van Beusekom, C. T. Lancee, G. Springeling, I. Krabbendam, A. F. van der Steen, R. Huber, and G. van Soest, "Heartbeat oct: in vivo intravascular megahertz-optical coherence tomography," *Biomed. Opt. Express* **6**, 5021–5032 (2015). [doi: 10.1364/BOE.6.005021].

First Author.

Biographies and photographs of the other authors are not available.